

Cite this: *J. Mater. Chem. C*, 2025, 13, 2172

# Investigating the effect of hydrothermal carbonisation reaction times on the photoluminescence of bio-oil-derived carbon polymer dots†

Lawrence A. Bruce,<sup>a</sup> Liam Desmond,<sup>b</sup> Abigail A. Seddon,<sup>a</sup> Leon Bowen,<sup>c</sup> Greg A. Mutch,<sup>b</sup> Anh N. Phan<sup>\*b</sup> and Elizabeth A. Gibson<sup>\*a</sup>

Carbon dots (CDs) have favourable properties such as broad spectral absorption, strong photoluminescence, low toxicity, and high specific surface area. Here, carbon polymer dots (CPDs), which are CDs with a carbon core and polymeric surface, were synthesised from chitin-derived bio-oil, supporting the transition away from fossil-based feedstocks in carbon nanomaterial synthesis. The influence of hydrothermal carbonisation (HTC) reaction times on the structural, morphological, and optical properties were studied. Structural analysis revealed the formation of nitrogen-doped CPDs with a cross-linked polymeric shell surrounding a crystalline graphitic carbon core, with the size, structure, and surface composition all influenced by HTC reaction time. All CPD samples showed the same excitation dependent emission, with a  $\lambda_{\text{max}}$  of 394 nm. Deconvolution of the photoluminescence showed multiple components with contributions identified from both molecular luminophores and the carbon core. Overall, this work investigates the mechanism of photoluminescence in CPDs, providing insights that could promote application in areas such as bioimaging, sensing, and optoelectronics.

Received 7th September 2024,  
Accepted 2nd December 2024

DOI: 10.1039/d4tc03858d

rsc.li/materials-c

## 1. Introduction

Carbon dots (CDs) are an emergent class of photoluminescent carbon nanomaterial, discovered in 2004 by Xu *et al.* during the purification of single-walled carbon nanotubes fabricated by arc-discharge from soot.<sup>1</sup> Their favourable properties such as broad spectral absorption,<sup>2</sup> strong photoluminescence,<sup>3</sup> tunable emission,<sup>4–6</sup> low toxicity,<sup>7,8</sup> conductivity,<sup>9</sup> and high specific surface area<sup>10</sup> have facilitated their application in biomedical sciences and as energy materials.<sup>11–13</sup> However, in the literature, the term “CDs” is often used to refer broadly to a range of carbon nanomaterials, which can vary significantly in structure and properties. The classification of CDs in the literature contains some discrepancies, CDs can be loosely classified into four categories (Table 1). More research is needed to elucidate mechanisms of formation and structure–activity relationships.<sup>6</sup> In particular, the influence of synthesis methodology on the size, structure, and optical properties of CDs is poorly understood.<sup>14</sup>

In this introduction, the term CD will be used collectively to refer to the broad range of carbon nanomaterials, including graphene quantum dots, carbon quantum dots, carbon nanodots, and carbon polymer dots, as classified in Table 1, to discuss the general trends observed in their structure, morphology, and properties.

Doping CDs with heteroatoms effectively tunes their electronic and optical properties. This can be achieved through in-plane substitution, intercalation, or surface replacement. Various heteroatoms are used such as boron, phosphorus, silicon, and metals.<sup>19,27</sup> For example, Zhai *et al.* (2012) found that increasing nitrogen content in CDs *via* microwave-assisted pyrolysis boosted the fluorescence quantum yield (QY) from 2.2% to 30.2%.<sup>28</sup> While Qian *et al.* (2014) observed that the incorporation of nitrogen atoms significantly boosted the QY of N-CQDs, achieving a maximum emission efficiency of 36.3%.<sup>29</sup>

Biomass (waste and residues) is abundant, low-cost and naturally incorporates dopants, making it a cost-effective method for synthesising doped CDs.<sup>30–32</sup> Improvements in photoluminescence have been observed where the enhanced nitrogen content contributes to increased QY and tunable optical properties by further functionalisation.<sup>33</sup> Chitin, a by-product of the fishing industry processed from prawn and crab shell waste, was selected for its high nitrogen content (~7 wt%).<sup>28</sup> Previously, Briscoe *et al.* (2017) synthesised a series of biomass derived CDs

<sup>a</sup> Energy Materials Laboratory, Bedson Building, Newcastle University, Edward's Walk, Newcastle upon Tyne NE1 8QB, UK. E-mail: anh.phan@newcastle.ac.uk, elizabeth.gibson@newcastle.ac.uk

<sup>b</sup> School of Engineering, Merz Court, University, Newcastle upon Tyne NE1 7RU, UK

<sup>c</sup> Durham University, Department of Physics, South Road, Co Durham, DH1 3LE, UK

† Electronic supplementary information (ESI) available. See DOI: <https://doi.org/10.1039/d4tc03858d>



**Table 1** The classification of CDs and their associated size, structure, and proposed mechanism of photoluminescence

Classification	Size (nm)	Structure	Photoluminescence
Graphene quantum dot (GQD) <sup>15</sup>	1–20	Crystalline, graphene lattice with sp <sup>2</sup> hybridised carbon domains. Functionalised groups on the edges and basal plane.	Quantum confinement <sup>16–18</sup> Edge effects <sup>17</sup> Surface states <sup>19,20</sup> Defects <sup>21</sup> Molecular fluorophores <sup>22</sup>
Carbon quantum dot (CQD) <sup>23</sup>	2–10	Quasi-spherical nanoparticles, crystalline carbon core and chemical groups on the surface (core-shell).	Quantum confinement <sup>24</sup> Core-shell structure <sup>24</sup> Surface states/defects Molecular fluorophores
Carbon nanodots (CNDs or C-dots) <sup>20</sup>	2–10	Amorphous nanoparticles highly carbonised sp <sup>3</sup> hybridised graphitic/turbostratic carbon core with groups on the surface (core-shell).	Quantum confinement Core-shell structure <sup>24</sup> Surface states/defects Molecular fluorophores
Carbonised polymer dots (CPDs) <sup>25</sup>	< 100	Carbon core (CQD or CND) with surface cross-linked or aggregated functional groups.	Core-shell structure Surface states/defects Cross-link enhanced emission <sup>26</sup> Conjugated $\pi$ -domain Molecular fluorophores

by hydrothermal carbonisation (HTC) at 200 °C for 6 h from glucose, chitin, and chitosan (the deacylated form of chitin) with corresponding quantum yield (QY) of 1.4%, 11.6% and 13.4%. The results demonstrate a notable improvement in QY with nitrogen-doped CDs.<sup>34</sup> Jiang *et al.* (2022) achieved an impressive QY of 54% from spheroidal CDs derived from chitin, synthesised *via* HTC at 240 °C for 10 h. These CDs had an average diameter of 4.2 nm. The X-ray diffraction (XRD) pattern displayed a broad peak at 23° ( $d_{002} = 0.34$  nm), indicating the presence of amorphous carbon. The photoluminescence was excitation-dependent, accredited to quantum confinement and surface states.<sup>35</sup> Chitin-CQDs have also been synthesised directly from prawn shells by (i) deproteinisation with NaOH (ii) demineralisation with HCl (iii) then HTC at 200 °C for 8 h. Transmission electron microscopy (TEM) and XRD analysis confirmed the presence of homogeneous spherical nanoparticles composed of amorphous carbon. Blue excitation dependent emission was recorded with a QY of 25.8%.<sup>36</sup> A literature review of CDs produced from chitin, chitosan, and combinations such as chitosan with *p*-phenylenediamine or  $\kappa$ -carrageenan by HTC was conducted (Table S1, ESI†). The operating conditions ranged from 180–220 °C with reaction times between 5–24 h. The size of the resulting CDs was between 0.5 nm and 20 nm. For the majority of the CDs, photoluminescence was attributed to surface emission sites and carbon cores. The emission wavelengths ( $\lambda_{\max}$ ) ranged from 400–to 533 nm, with QY up to 59%. Lifetimes, reported in nanoseconds, reflected complex decay profiles, indicating multiple emissive states. More research is required to understand the structure–property relationships of CDs; particularly the mechanisms underlying their photoluminescence, which could lead to enhanced control over their optical properties for optoelectronic applications.<sup>6,37</sup> Challenges persist in the synthesis of biomass-derived carbon CDs as the varying composition of different biomass sources results in inconsistencies in their properties. Determining the optimal synthetic conditions, such as temperature, reaction time, pH, and precursor concentration is crucial. Additionally, the mechanism of CD formation from biomass remains unclear, highlighting the need for methods to

control and modify CD properties more effectively. In this work, nitrogen doped carbon polymer dots (N-CPDs) were synthesised from chitin.<sup>38</sup> N-CPDs were synthesised from the crude bio-oil derived from the pyrolysis of chitin, followed by HTC. The synthesised dots were classified as carbon polymer dots (CPDs) due to their size (17–45 nm) and morphology. The reaction time of the hydrothermal treatment was varied to examine how changes in morphology, chemical composition, and structure affected the photoluminescence. The proposed formation mechanism involves pyrolysis degrading chitin into a mixture of nitrogen (N) & oxygen (O) containing heterocyclics and small molecules, with high temperature (700 °C) being sufficient to induce graphitization.<sup>4</sup> During the HTC, these fragments serve as nucleation sites for cross-linking polymerisation, where dehydration and condensation reactions lead to the formation of a cross-linked polymeric shell around the carbon core.<sup>39–42</sup>

Photoluminescence was found to have contributions from both the crystalline carbon core and a luminescent molecule; namely 3-aminopyridine.<sup>43–45</sup> Overall, our work demonstrates that bio-oil derived from chitin can serve as an efficient feedstock for producing nanomaterials. This work introduces a methodology that can be extended to other bio-oil streams, offering a versatile approach for producing nanomaterials from various bio-oil sources (including waste). This approach provides benefits such as resource efficiency, carbon sequestration, and reduced environmental impact.<sup>46</sup> Utilising biomass waste aligns with the circular economy, which prioritises resource reuse and waste minimisation according to the waste hierarchy.<sup>47,48</sup>

## 2. Results

### 2.1. Synthesis of N-CPDs

Chitin was pyrolysed at 700 °C in an inert atmosphere to produce a biochar (~35%), liquid known as bio-oil (~50%), and gas (~15%). This temperature was selected to ensure complete conversion of the biomass and achieve a sufficiently high bio-oil yield.<sup>49</sup> A temperature of 700 °C was found to give a



higher yield of bio-oil than 450 °C (~36%) (Table S2, ESI†). Analysis of the bio-oil produced at 700 °C by gas chromatography mass spectrometry (GC-MS) showed that acetic acid and acetamide were the dominant products formed (Fig. S1, ESI†). The production of large amounts of acetic acid was expected due to the hydrolysis of the acetyl amide side chain. A large mixture of O and N-heterocyclics were observed (Table S3, ESI†), which is consistent with other work.<sup>50</sup>

The bio-oil was further processed by HTC at 200 °C over various holding times to understand the effect of reaction time on the product's structure, morphology, surface chemistry, and photoluminescence. Typical HTC temperatures for chitosan/chitin CD synthesis range from 180–220 °C.<sup>32</sup> The temperature of 200 °C was chosen to ensure the efficient formation of the N-CPDs while avoiding excessive thermal degradation. A midpoint of 200 °C facilitated the comparison with previously synthesised chitin/chitosan derived CDs. The reaction time was varied from 2, to 4, and 8 h, with resulting samples labelled 2H-CPD, 4H-CPD, and 8H-CPD, respectively. After the HTC reaction, the N-CPDs were purified by filtration, followed by centrifugation, and solvent extraction with ether to remove impurities. Previous experiments incorporated an additional step of dialysis; however, it had no discernible effect on the purification process. The aqueous fraction containing the N-CPDs was freeze-dried and afterwards washed and sonicated with ether again until the solid N-CPDs crashed out of solution. This protocol was developed to ensure that no impurities or residual solvents are adsorbed onto the surface or trapped within the structure of

the N-CPDs during freeze-drying. Vigorous purification, including centrifugation, filtration, and solvent extraction is essential to ensure accurate characterisation of the luminescence as it eliminates byproducts that can otherwise distort the true emission properties.<sup>51</sup>

During the purification of the N-CPDs, the organic fraction (ether) containing impurities was isolated from the solvent extraction for each sample (2H-CPD, 4H-CPD, and 8H-CPD). The fractions were analysed by GC-MS, and a mixture of ketone, phenol and pyridine derivatives were observed. 3-Acetamidopyridine was present in all the fractions and bio-oil (Table S4: 2H-CPD, Table S5: 4H-CPD, and Table S6: 8H-CPD, ESI†). The maximum yield from bio-oil to N-CPDs (8.8%) occurred at 8 h HTC time (Table S7, ESI†). The overall yield of chitin to N-CPDs was 4.5%. The N-CPDs were hygroscopic, which was attributed to their abundant hydrophilic surface groups, small size with a high surface area, and a potential crosslink-enhanced effect that allows them to effectively bind and retain water molecules.<sup>52</sup> All the samples were found to be hydrophilic; easily dispersing in water and with a zeta potential of –15 mV.

## 2.2. Morphology and structure of N-CPDs

TEM images of N-CPDs synthesised with HTC reaction times of 2, 4, and 8 h are shown in Fig. 1. The TEM results confirmed the synthesis of nanoscale N-CPDs by pyrolysis followed by HTC. The images collected show the overall size of the N-CPDs, including both the crystalline carbon core and the amorphous cross-linked polymeric shell. Due to the size and the structure,

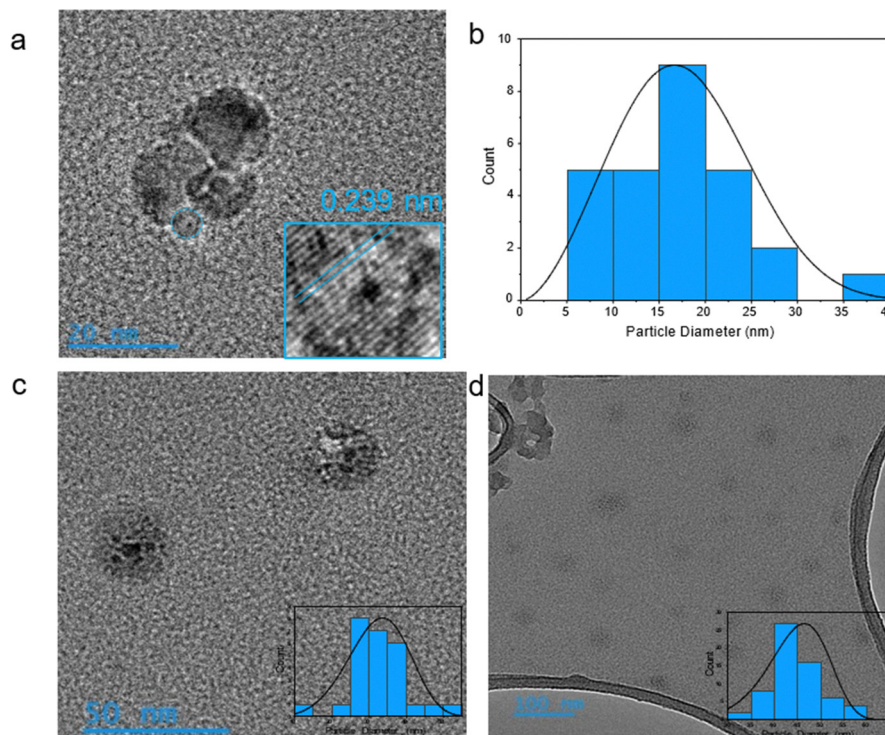


**Fig. 1** N-CPD samples were prepared for TEM by dispersion in IPA and sonication, before deposition on a carbon grid. (a) TEM image of 2H-CPD and (inset) magnification showing the crystal lattice grating, and (b) size-distribution from TEM analysis of 2H-CPD. TEM image and size distribution for (c) 4H-CPD and (d) 8H-CPD. The size distributions were determined from averaging all imaged N-CPDs.



the synthesised nanomaterials were classified as CPDs. Fig. 1a shows the N-CPDs had a uniform spherical morphology and were well dispersed, with some agglomeration in the 2H-CPD sample. Additionally, the TEM images show an increase in the average particle size as the reaction time increased; 2H-CPD:  $(17 \pm 7)$  nm, 4H-CPD:  $(33 \pm 8)$  nm, and 8H-CPD:  $(45 \pm 6)$  nm.

In Fig. 1a, a crystal lattice spacing of 0.23 nm was calculated corresponding to the reported (100) crystal facet of graphite.<sup>53,54</sup> The crystal lattice was not observed by TEM for 4H-CPD or 8H-CPDs, consistent with the Raman spectroscopy in Fig. 2. CPDs synthesised from HTC by bottom-up processes typically exhibit lattice spacings incomparable with the graphite/graphene lattice due to the polymeric or ordered polymer/carbon hybrid structure.<sup>26,42</sup> Luo *et al.* (2022)<sup>55</sup> demonstrated that CDs synthesised *via* HTC at temperatures above 350 °C under an inert atmosphere led to structural instability, resulting in carbonisation. The process resulted in the removal of weakly bonded oxygen-containing functional groups and the formation of the conjugated sp<sup>2</sup> carbon to generate graphitic planes.<sup>55</sup> It was reasoned that the crystalline core formed during the pyrolysis step, as the pyrolysis temperature of 700 °C was sufficient to induce the crystallisation observed in the TEM images (Fig. 1a). Small fragments of graphitic carbon present in the bio-oil likely acted as nucleation sites during HTC, where their growth was facilitated by increased hydrothermal cross-linking polymerisation. At extended reaction times, the dehydration of functional groups in the precursors, driven by intramolecular collisions, promoted the formation and extension of polymer chains with cross-links. This process led to the development of a polymeric cross-linked shell that enveloped the pre-formed crystalline carbon core.<sup>42</sup> It was rationalised that the increase in size was due to more extensive hydrothermal cross-linking reactions occurring at longer reaction times, leading to the growth of a larger cross-linked polymeric structure.

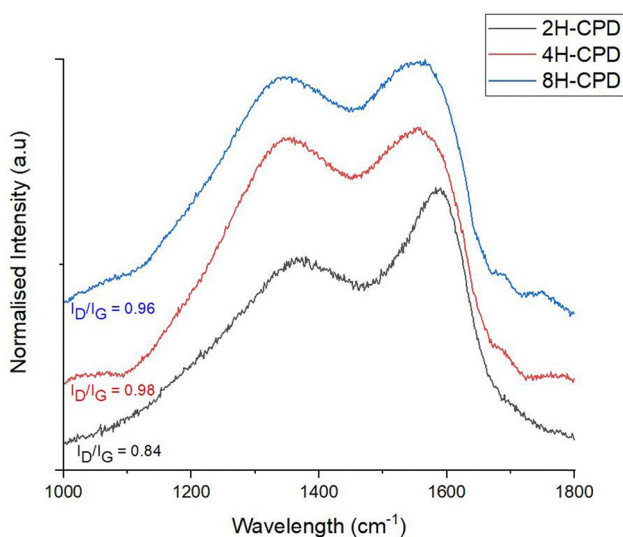


Fig. 2 Analysis of Raman spectroscopy data related to the D-band and G-bands; data was processed by a 2-point baseline correction then normalised. The excitation wavelength was at 532 nm with a grating 600 g mm<sup>-1</sup>.

The collection of XRD data was limited by the need for a larger material quantity, and the hygroscopic nature also complicated handling and preparation of dry samples. Additionally, the N-CPDs contained a mixture of amorphous and crystalline regions, with limited crystalline content that is often too small or disordered to produce distinct XRD peaks. This is consistent with similar studies, where broad, weak peaks are observed in XRD for amorphous materials, contributing little beyond the information from Raman spectroscopy and TEM.<sup>35,56,57</sup>

### 2.3. Vibrational spectroscopy

Raman spectroscopy was used to further investigate the effect of reaction time on structural properties (Fig. 2). Raman scattering is sensitive to highly symmetric covalent bonding with no or little natural dipole moments. Therefore, it is an insightful technique to use for carbon-carbon bonds in nanomaterials as slight changes in the structure can be discerned. Of interest is the D-band (disordered band  $\approx 1350$  cm<sup>-1</sup>), originating from the hybridised vibrational mode associated with dangling bonds, edge effects and structural defects (*i.e.*, disordered carbon).<sup>58</sup> The G-band (1580 cm<sup>-1</sup>) is attributed to the in plane vibrational mode of the of sp<sup>2</sup>-bonded carbon atoms in the hexagonal lattice, associated with graphene and graphite. The relative intensity ratio of the D- and G bands ( $I_D/I_G$ ) is used to measure the relative defect density. 2H-CPD showed a D-band at 1369 cm<sup>-1</sup> and a G-band at 1586 cm<sup>-1</sup>. As the reaction time increased, a discernible change in structure was signalled by a downward shift of the G-band to lower wavenumbers, observed in samples 4H-CPD: 1556 cm<sup>-1</sup> and 8H-CPD: 1555 cm<sup>-1</sup>. The  $I_D/I_G$  of 0.84 for 2H-CPD is consistent with crystalline character with a degree of disorder (Fig. 2).<sup>59</sup> The breadth of the D band also indicates disorder in the aromatic cluster. As the reaction time was increased, the intensity of the D band increased for both 4H-CPD and 8H-CPD. The  $I_D/I_G$  of 0.98 for 4H-CPD and 0.96 for 8H-CPD is consistent with a decrease in the crystallinity as the reaction time increased. Previous studies have shown that longer HTC reaction times lead to increased crystallinity.<sup>39,60</sup> Ehrat *et al.* (2017) synthesised CDs from citric acid and ethylenediamine by HTC from 15 min to 10 h. As the reaction time increased, the initially formed molecular fluorophores acted as nucleation seeds for the growth of aromatic domains, resulting in enhanced crystallinity.<sup>60</sup> However, in this study as the HTC reaction time increased, the amount of graphitic character decreased 2H-CPD:  $I_D/I_G = 0.84$ , 4H-CPD:  $I_D/I_G = 0.98$  and 8H-CPD  $I_D/I_G = 0.96$  (Fig. 2). This was attributed to by the increasing size of the CPD from 2H-CPD:  $(17 \pm 7)$  nm to 8H-CPD:  $(45 \pm 6)$  nm (Fig. 1) and the increased size of the disordered cross-linked polymeric shell that grew during the HTC by hydrothermal cross-linking polymerisation.

The Fourier transform infrared FT-IR spectrum (Fig. 3a) confirmed the transformation of the starting material chitin to N-CPDs. The N-CPD samples (Fig. 3b) all showed a strong and broad O-H stretch from 3600–3200 cm<sup>-1</sup>. Additionally, the N-H stretch (3200–3180 cm<sup>-1</sup>), N-H bending (1560 cm<sup>-1</sup>) and C-N bending (1310 cm<sup>-1</sup>) were retained. The sharp amide carbonyl stretching (C=O) mode at  $\sim 1660$  cm<sup>-1</sup> was also retained, however, at longer HTC reaction time, the amide



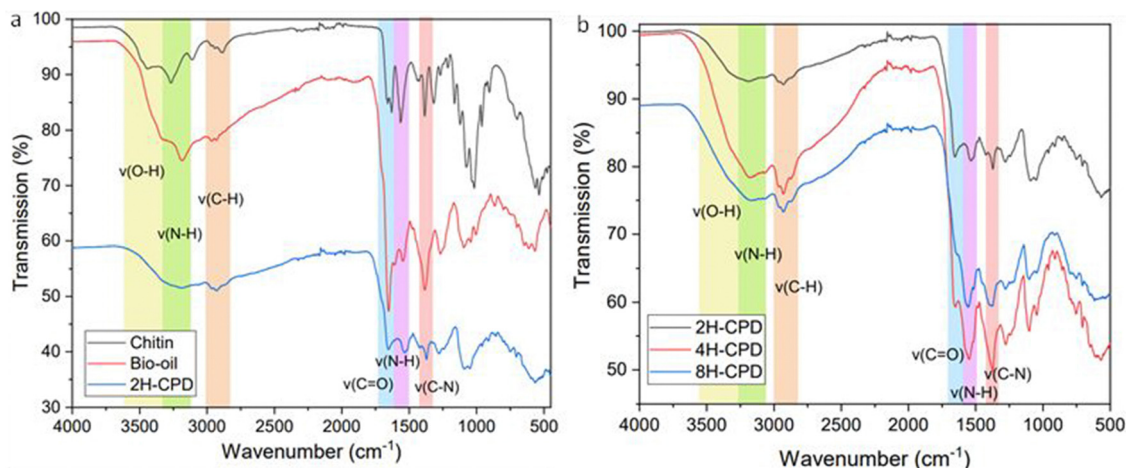


Fig. 3 (a) FT-IR spectra of chitin, bio-oil derived from the pyrolysis of chitin at 700 °C, and nitrogen doped CPDs synthesised from HTC at 200 °C (2H-CPD) (b) FT-IR spectra of nitrogen doped CPDs synthesised at 200 °C HTC at 2 h (2H-CPD), 4 h (4H-CPD), and 8 h (8H-CPD).

peak became weaker from 2H-CPD to 8H-CPD (Fig. 3b). This was consistent with the X-ray photoelectron spectroscopy (XPS) analysis of the surface composition of the CPDs (Fig. 4).

#### 2.4. X-ray photoelectron spectroscopy

The elemental composition of carbon and nitrogen for the N-CPDs samples was found to remain consistent, with a nitrogen

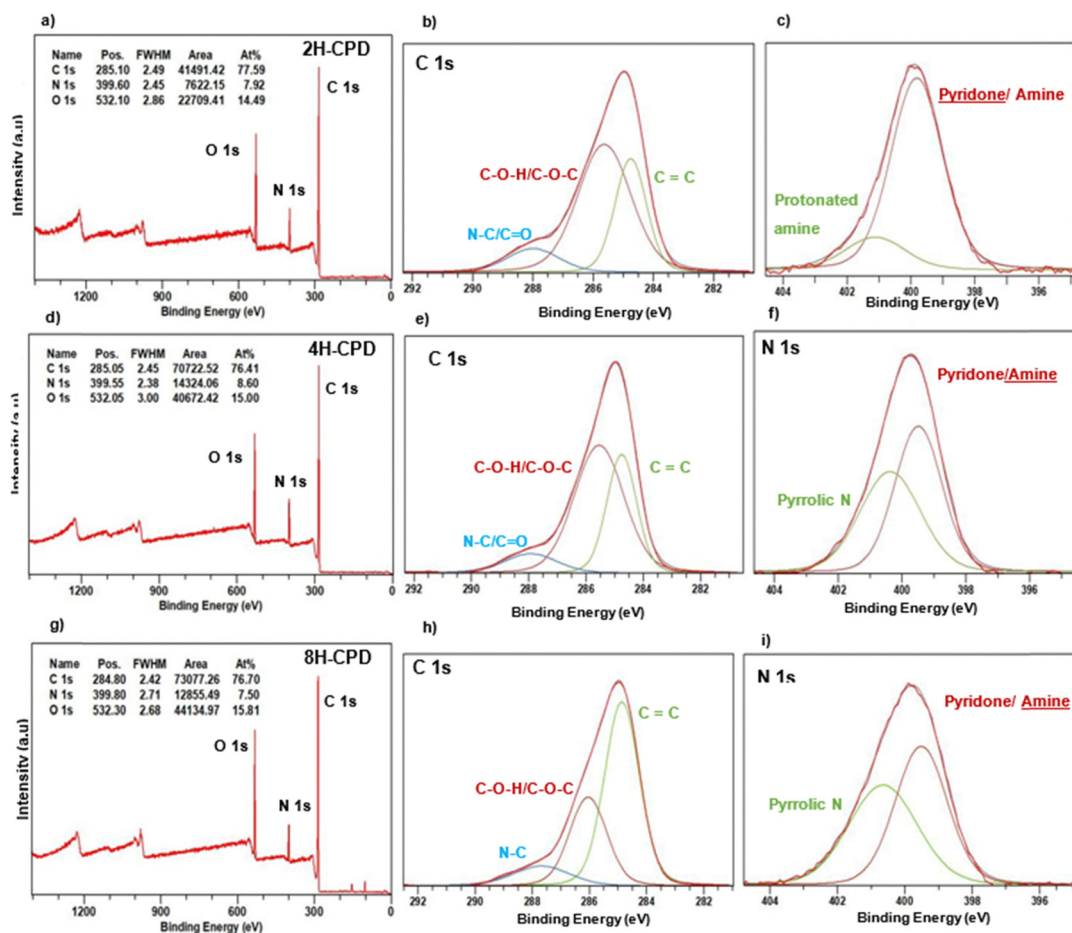


Fig. 4 Row (a) 2H-CPDs, from left elemental composition, C 1s fitted XPS spectrum, and N 1s fitted spectrum. Row (b) 4H-CPDs, from left elemental composition, C 1s fitted XPS spectrum, and N 1s fitted spectrum. Row (c) 8H-CPDs, from left elemental composition, C 1s fitted XPS spectrum, and N 1s fitted spectrum.



Table 2 Summary of peak assignments and corresponding binding energy (eV) and peak area (%) for C 1s and N 1s for all N-CPD samples

Sample	C 1s			N 1s		
	Peak	Binding energy (eV)	Area (%)	Peak	Binding energy (eV)	Area (%)
2H-CPD	C=C	284.8	30.3	O=CNC/H-N-H	399.8	83.44
	C-O-H/C-O-C	265.6	59.1	C-NH <sup>+</sup> /Hydrogen Bonded	401.1	16.56
	C-N	288.0	10.5			
4H-CPD	C=C	284.8	32.3	O=C-N-C/H-N-H	399.5	53.2
	C-O-H/C-O-C	285.6	58.4	C-(NH)-C	400.4	46.8
	C-N	287.9	9.3			
8H-CPD	C=C	284.9	59.0	O=C-N-C/H-N-H	399.5	48.5
	C-O-H/C-O-C	285.1	30.6	C-(NH)-C	400.7	51.5
	C-N	287.7	10.4			

composition (7.5–8.6%) larger than the nitrogen content found from CHN analysis of the starting reagent chitin (6.57%). The oxygen composition increased with longer reaction times (2H-CPD: 14.5%, 4H-CPD: 15.0%, and 8H-CPD: 15.8%).

For 2H-CPD, three peaks were observed in the C 1s region (Table 2) at 284.8, 265.6, and 287.9 eV which were assigned to C=C, C-O-H/C-O-C, and C-N respectively.<sup>46,53</sup> In the N 1s region there is a peak at 399.8 eV which was assigned to O=C-N/H-N-H, and is characteristic of a pyridone/amine group.<sup>61–63</sup> Of the total N 1s peak area, the contribution from O=C-N/H-N-H functional groups was calculated to be ~83%. The remaining ~17% was assigned to H-N-H protonated amine at 401.1 eV.<sup>53,62,64,65</sup> This was confirmed by the N-H stretch (3200–3180 cm<sup>-1</sup>), N-H bending (1560 cm<sup>-1</sup>) and C-N bending (1310 cm<sup>-1</sup>) in the FT-IR (Fig. 3). For 4H-CPD, the C 1s spectrum closely resembled that of 2H-CPD. However, in the N 1s spectrum, a distinct peak at 400.4 eV was observed, which was attributed to pyrrolic nitrogen.<sup>61</sup> Additionally, a shift of the pyridone/amine peak to 399.5 eV was observed, along with a decrease in the intensity of the amide (C=O) mode around

1660 cm<sup>-1</sup> in the FT-IR (Fig. 3). The peak showed a more significant amine contribution.<sup>61,66</sup> For 8H-CPD the C 1s peak area of the C=C functional group significantly increased to 59.0% from 32.3% in 4H-CPD. The N 1s remained consistent in assignment, position, and distribution of peak area with 4H-CPD, with a further decrease observed in the sharpness of the amide (C=O) mode. After the 8 h HTC the cross-linked polymeric structure is still intact, and full carbonisation hasn't yet occurred as confirmed by XPS (Table 2). The C 1s peak area at 2 h and 4 h was predominantly composed of C-O-H/C-O-C bonds, accounting for 59.1% and 58.4%, respectively. Interestingly, after 8 h HTC it appears as though the process of cross-linked polymer to amorphous carbon is starting to occur. From 2 h to 8 h there is an increase in the amount of C=C bonds on the surface from 30.3% to 59.0%.

## 2.5. Optical properties

The UV-visible spectra of all three N-CPD samples (Fig. 5a and Fig. S5, ESI†) contained two broad peaks at approximately 280 nm corresponding to the  $\pi \rightarrow \pi^*$  transition of the aromatic

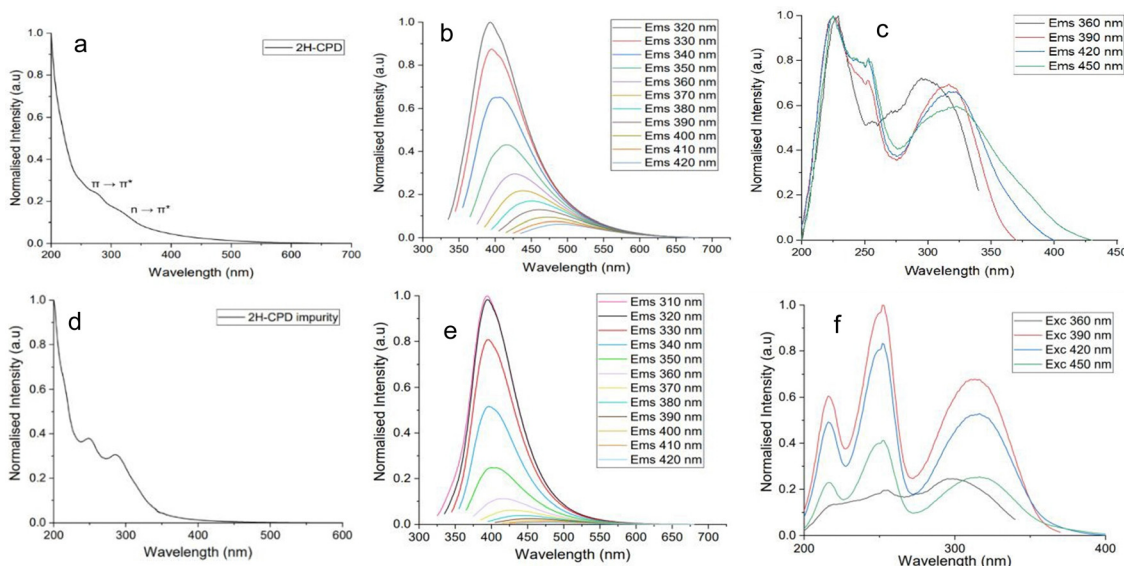


Fig. 5 (a) absorbance, (b) excitation-dependent photoluminescence and (c) excitation spectra for 2H-CPD. 2H-CPDs were synthesised from the 2H HTC of chitin-derived bio-oil, they dispersed in deionised water and were sonicated for 20 minutes prior to measurements. (d) absorbance, (e) photoluminescence and (f) excitation spectra for the impurity fraction isolated after the 2H HTC. The fraction was dispersed in deionised water and was sonicated for 20 minutes prior to measurements.



**Table 3** Summary of maximum emission wavelength ( $\lambda_{\text{max}}$ ), the quantum yield (QY), and lifetimes ( $\tau$ ). Quantum yield measurements were recorded at 320 nm and calculated relative to quinine sulphate in 0.5 M  $\text{H}_2\text{SO}_4$  which has a QY of 0.54. Photoluminescence lifetimes were recorded at an excitation wavelength of 440 nm

Sample	$\lambda_{\text{max}}$ (nm)	QY (%)	$\tau_1$ (ns)	$\tau_2$ (ns)
2H-CPD	394@320	6	$4.44 \pm 0.03$ (61%)	$12.44 \pm 0.08$ (28%)
4H-CPD	394@320	7	$4.65 \pm 0.04$ (62%)	$12.64 \pm 0.09$ (28%)
8H-CPD	394@320	8	$4.90 \pm 0.04$ (62%)	$12.94 \pm 0.09$ (28%)

$\text{sp}^2$  domains,<sup>67</sup> and at 320 nm corresponding to a  $n \rightarrow \pi^*$  transition ( $\text{C}=\text{O}$ ).<sup>68,69</sup> The absorption occurring at longer wavelengths was assigned to the energy level transitions from the conjugated  $\pi$ -structure.<sup>69</sup> Strong photoluminescence was recorded in the blue and visible regions of the emission spectrum, and photoluminescence was excitation wavelength dependent, with a red shift as the excitation wavelength increased. The maximum emission wavelength ( $\lambda_{\text{max}}$ ) was 394 nm at an excitation wavelength of 320 nm (Fig. 5b and Table 3). Excitation spectra were measured to examine the absorption characteristics of the emissive state. The consistent structure of the peaks suggests the excitation of a similar emissive state (Fig. 5c and Fig. S5, ESI<sup>†</sup>). The photoluminescence decay was fitted to two exponential components, which were within the timescale ( $\sim 1$ –10 ns) (Table 3). This is consistent with previously reported CDs (Table S7, ESI<sup>†</sup>).<sup>25,70</sup> The optical properties of all N-CPDs samples were identical (Fig. S2, ESI<sup>†</sup>).

To investigate further whether an independent fluorophore contributed to the photoluminescence, the optical properties of the organic fraction containing impurities from the purification step was recorded and compared to that of the N-CPDs (Fig. 5). The optical properties of the organic fraction containing impurities remained consistent irrespective of the duration of the

HTC reaction (Fig. S3, ESI<sup>†</sup>). The UV-vis spectra contained two peaks, at 250 nm and 280 nm, with a small tail extending into the visible spectrum. The maximum emission wavelength ( $\lambda_{\text{max}}$ ) was 394 nm at an excitation wavelength of 310 nm. From an excitation wavelength of 310 nm to 350 nm, the emission is excitation-independent with a  $\lambda_{\text{max}}$  of 394 nm. However, from 360 nm excitation-dependent emission is observed corresponding with the beginning of the tail in the absorption spectra (Fig. 6d). Excitation spectra were recorded from an emission wavelength of 390–450 nm; the spectra are the same suggesting a similar emissive state. However, at an emission wavelength of 360 nm the excitation spectrum looks more like the absorption observed in Fig. 6d with peaks at 250 nm and 280 nm (Fig. 6f).

Gaussian deconvolution of the photoluminescence for both the N-CPDs and the isolated impurity was performed to identify the components contributing to the overall photoluminescence (Fig. 6). A large contribution to the total photoluminescence at an excitation wavelength 320 nm for the N-CPD shared a considerable overlap with the emission of the isolated impurity at the same wavelength. An additional small and broad component was identified in the N-CPD that was attributed to the contribution from the N-CPD. At an excitation wavelength of 370 nm, the contribution from a molecular luminophore in the isolated impurity remained, contributing strongly to the overall photoluminescence of the N-CPD. An additional component was observed at 2.5 eV (495 nm). At an excitation wavelength of 420 nm the Gaussian deconvolution of both the N-CPD and isolated impurity appeared identical.

GC-MS analysis of the organic fraction containing impurities consistently revealed the presence of 3-aminopyridine. The photoluminescence of 3-aminopyridine exhibited optical properties similar to the synthesised N-CPDs. The photoluminescence

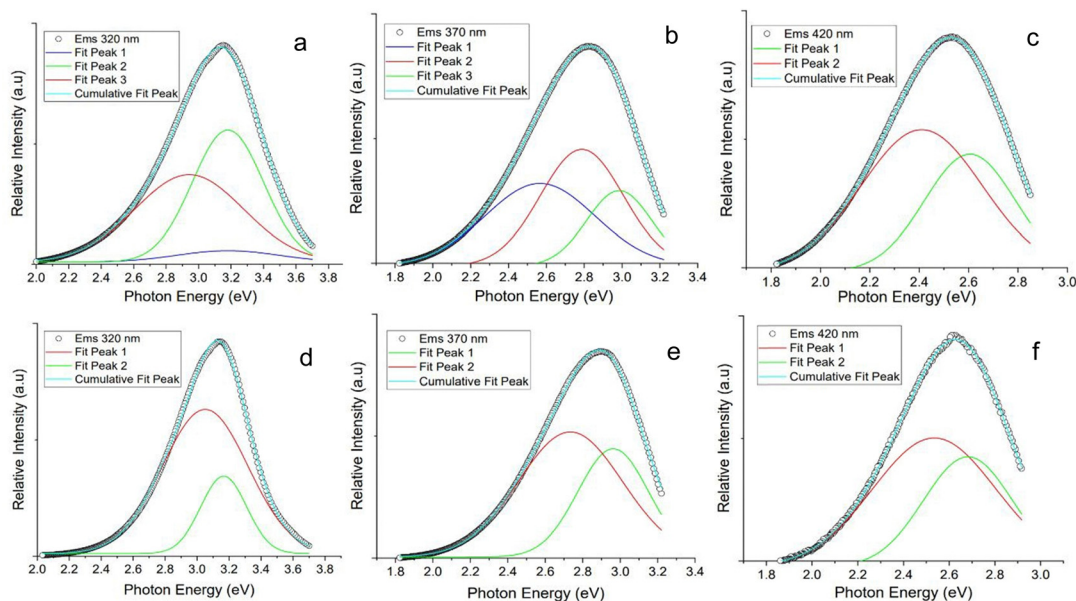


**Fig. 6** Gaussian peak fitting of photoluminescence data of 2H-CPDs synthesised from the 2H HTC of chitin-derived bio-oil, with excitation wavelengths of (a) 320 nm, (b) 370 nm, and (c) 420 nm. Gaussian peak fitting of photoluminescence data of the impurity fraction isolated after the 2 h HTC, with excitation wavelengths of (d) 320 nm, (e) 370 nm, and (f) 420 nm.



of 3-amino pyridine was characterised in deionised water with absorption  $\lambda_{\text{max}}$  of 215, 233 nm and at 290 nm, and a  $\lambda_{\text{max}}$  emission of 390 nm when excited at 320 nm (Fig. S4, ESI†).<sup>43,45</sup>

Photoluminescence in CPDs has been attributed to several factors including interactions from the core-shell structure, surface states, defects, cross-link enhanced emission, conjugated  $\pi$ -domains and from molecular fluorophores.<sup>26,42</sup> A contribution from a surface state was neglected; we rationalised that an observable change in the photoluminescence would be seen corresponding to the changing surface composition observed in the XPS (Fig. 4). The deconvolution of the photoluminescence (Fig. 6) revealed the presence of multiple peaks, confirming the existence of numerous photoluminescent centres. A large contribution to the overall photoluminescence of the N-CPDs from a molecular luminophore was observed. Previously, Song *et al.* (2015) identified multiple photoluminescent centres for CDs; IPCA (imidazo[1,2-*a*]pyridine-7-carboxylic acid, 1,2,3,5-tetrahydro-5-oxo-), a bright blue fluorophore, and its derivatives were found to contribute to a molecular state photoluminescence in the CDss. In addition, they found a weaker contribution originated from carbon core, consisting of nano-sized carbon cores and polymeric clusters.<sup>71</sup>

Emission occurring from the crystalline carbon core has been characterised as having intrinsic and extrinsic emission. Intrinsic emission has strong blue emission at 400 nm when excited near 325 nm. It originates from the minimally oxidised and low defect isolated  $\text{sp}^2$  hexagonal carbon domains.<sup>72,73</sup> Yoon *et al.* (2016) investigated the origin of this intrinsic luminescence by investigating the subdomain formation. They found that the preferential size of the sub-domain was a cluster of four to seven carbon hexagons isolated by oxygen containing functional groups forming stable formations of subdomains. Extrinsic emission has been described as emission occurring at 500 nm when excitation at 325 nm and above, resulting from excessive defects, including oxygen functional groups.<sup>72</sup>

A  $\lambda_{\text{max}}$  of 394 nm for emission at an excitation wavelength 320 nm was observed for all N-CPD samples, which is close to the value reported for intrinsic emission. However, the deconvolution of the photoluminescence and comparison with the isolated impurity would suggest that this is coming from a molecular luminophore as opposed to the carbon core itself. A smaller and broader component was attributed to the contribution from the carbon core (Fig. 6). An explanation for the excitation-dependent emission observed in the N-CPD was attributed to the quantum confinement of differently sized  $\pi$ -conjugated sub-domains within the crystalline core. Size dependent photoluminescence would be expected due to the energy gap transitions from the quantisation of the  $\pi$ -conjugated system, with a red-shift observed as larger sub-domains form. The broadness of the observed peak can be explained by a large distribution of sub-domains.<sup>74,75</sup> The predominant source of the overall photoluminescence in the N-CPDs was primarily associated with a molecular luminophore, 3-aminopyridine, alongside a lesser contribution from sub-domains within the crystalline carbon core. However, XPS analysis did not confirm the presence of 3-aminopyridine on the surface (Table 2), as no peak corresponding to the pyridine (C=N-C) bond was observed in the 397.8–398.8 eV range.<sup>61</sup> The absence of

this peak suggests that either the concentration of 3-aminopyridine on the surface is too low to be detected, or that it is embedded within the cross-linked polymeric matrix. The rigorous purification protocol significantly reduces the likelihood that the observed photoluminescence is due to surface contamination. Emphasising the need for vigorous purification to accurately characterise the true mechanism of photoluminescence.

### 3. Conclusion

Overall, the findings of this study underscore the potential of utilising bio-oil for the sustainable synthesis of carbon nanomaterials and contributes to a deeper understanding of their structure-property relationships. N-CPDs were synthesised from pyrolysis of chitin followed by hydrothermal treatment, introducing the potential of using a waste stream, bio-oil, for the synthesis of N-CPDs. The effect of HTC reaction time on the size, structure, surface composition, and optical properties was explored. Longer reaction times led to the formation of larger N-CPDs with a polymeric cross-linked shell surrounding a crystalline graphitic carbon core. The proposed formation mechanism involves pyrolysis degrading chitin into smaller fragments, with the temperature being sufficient to induce graphitization. These fragments then serve as nucleation sites for hydrothermal cross-linking polymerization, resulting in the creation of a cross-linked polymeric structure. At longer HTC reaction times, this structure gradually carbonises. Interestingly, although the size, structure, and surface composition were noted to change as the reaction time increased, the observed optical properties remained consistent. The optical properties of N-CPDs were thoroughly characterised, revealing strong photoluminescence in the blue and visible regions of the spectrum. Excitation wavelength-dependent emission and multi-component photoluminescence spectra were observed, indicating the presence of diverse photoluminescent centres. Gaussian deconvolution analysis suggested contributions from both a molecular luminophore (3-amino pyridine) and the carbon core to the overall photoluminescence. Future work could investigate alternative bio-oil sources and how surface modifications of N-CPDs influences their photophysical properties. Nuclear magnetic resonance spectroscopy,  $^1\text{H}$  NMR and  $^{13}\text{C}$  were not performed due to the complex surface chemistry of the N-CPDs, with mixed functional groups and cross-linked structures, would likely lead to convoluted  $^1\text{H}$  NMR and  $^{13}\text{C}$  NMR spectra, making interpretation difficult. By enhancing or tailoring the optical properties, CPDs could become more suitable for applications in energy materials. The consistent photoluminescent properties and reasonable QY provide a solid foundation for further improvements and potential advancements in this field.

### 4. Experimental methodology

#### 4.1. Materials

Chitin, diethyl ether, and acetonitrile ( $\geq 99.9\%$ , gradient grade, suitable for HPLC) were purchased from Merck. 2-Acetamidophenol, 3-amino pyridine, 1-octanol, isoamyl ether,



and methyl laurate were purchased from Sigma Aldrich. 3-Acetamidopyridine was purchased from Combi-blocks. 0.22  $\mu\text{m}$  PTFE hydrophilic filter was purchased from Fisher Scientific.

#### 4.2. Method

N-CPDs were synthesised from chitin by pyrolysis at 700  $^{\circ}\text{C}$  (heating rate  $\sim 10^{\circ}\text{C min}^{-1}$ ) for 2 h under a  $\text{N}_2$  atmosphere to produce bio-oil and bio-char. Bio-oil (10 mL) was transferred to a Teflon-lined autoclave for hydrothermal treatment, water (30 mL, ratio 1 : 3 biomass : water). The autoclave was heated in an oven at 200  $^{\circ}\text{C}$ , and the reaction times were 2, 4, and 8 h. The reaction mixture was filtered through a Buckner funnel to collect a black precipitate. The resulting filtrate was then centrifuged at 4000 rpm for 15 minutes then filtered through a 0.22  $\mu\text{m}$  PTFE hydrophilic filter. The solution was then extensively washed with ether. The total volume of the solution was reduced by rotary evaporation and then freeze dried for 48 h. A brown viscous oily solid was obtained. This solid was washed with ether and sonicated until a brown powder crashed out of solution. The N-CPDs were noted to be hygroscopic, with little contact with water formed a viscous oil.

#### 4.3. Characterisation

Analysis using gas chromatography mass spectrometry (GC-MS) was conducted utilising an Agilent 8890 Chromatograph, which was fitted with an HP-5 capillary column (30 m  $\times$  0.25 mm, 0.25  $\mu\text{m}$  film thickness), and a 5977 MSD mass spectrometer. Transmission electron microscopy was performed using a JEOL 2100F operated at 200 keV. For the Raman spectra, a Horiba LabRAM HR Evolution spectrometer was used with an exciting line wavelength  $\lambda = 532$  nm, source power 455 mW. To attenuate the power at the sample, a non-dispersive filter was used reducing it to around  $\sim 1\%$  of the laser power. An Olympus LMPLFLN20X magnification objective was used to examine the samples. FT-IR was recorded on a PerkinElmer spectrum two FT-IR spectrometer. The XPS analysis was conducted using a Thermo NEXSA system equipped with a monochromated Al  $\text{K}\alpha$  X-ray source (1486.7 eV), with a spherical sector analyser, and three multichannel resistive plate detectors, each with a 128-channel delay line. All data were recorded at 19.2 W with an X-ray beam size of 400  $\times$  200  $\mu\text{m}$ . Absorption spectra were recorded on a Shimadzu UV-1800 spectrophotometer UV-vis and luminescence spectra were recorded on a Shimadzu RF-6000 spectrofluorophotometer. Luminescence spectra and excited-state lifetimes were measured using an Edinburgh FLS980 photoluminescence spectrometer, equipped with a 450 W Xenon arc lamp, Czerny Turner excitation and emission monochromators (1.8 nm  $\text{mm}^{-1}$  dispersion; 1800 grooves per mm), time-correlated single photon counting (TCSPC) module and a Hamamatsu R928P photomultiplier tube (in a fan assisted TE cooled housing, operating temperature  $-20^{\circ}\text{C}$ ). For lifetime measurements, samples were excited with an EPL-375 (370.8 nm; 61.1 ps pulse width) and an EPL-475 (471.8 nm; 61.1 ps pulse width) picosecond pulsed diode lasers and data analysis was performed on the F980 software with numerical data. A LECO CHN628 combustion elemental carbon, hydrogen, and nitrogen analyser was used to determine the

composition of the samples. The Zeta potential was measured with a Zetasizer Nano ZS Instrument (Malvern Panalytical Ltd).

## Author contributions

Lawrence Bruce: conceptualisation (ideas), methodology, investigation, writing – original draft, visualisation. Liam Desmond: conceptualisation (ideas), methodology, investigation. Abigail Seddon: methodology. Leon Bowen: resources, investigation. Greg. A. Mutch: funding acquisition, resources, writing – review & editing. Anh Phan: conceptualisation (of project), funding acquisition, supervision, writing – review & editing. Elizabeth A. Gibson: conceptualisation (of project), funding acquisition, supervision of LB and AS, writing – review & editing.

## Data availability

The data supporting the findings of this study are available upon reasonable request.

## Conflicts of interest

There are no conflicts to declare.

## Acknowledgements

This work was supported by the Engineering & Physical Sciences Research Council [grant numbers EP/V047078/1, EP/W03395X/1, EP/Y034961/1, EP/S023836/1, EP/R51309X/1]. GAM was supported by the Royal Academy of Engineering under the Research Fellowship scheme.

## References

- X. Xu, R. Ray, Y. Gu, H. J. Ploehn, L. Gearheart, K. Raker and W. A. Scrivens, *J. Am. Chem. Soc.*, 2004, **126**, 12736.
- L. Li, G. Wu, G. Yang, J. Peng, J. Zhao and J.-J. Zhu, *Nanoscale*, 2013, **5**, 4015.
- D. Qu, M. Zheng, P. Du, Y. Zhou, L. Zhang, D. Li, H. Tan, Z. Zhao, Z. Xie and Z. Sun, *Nanoscale*, 2013, **5**, 12272.
- H. Luo, N. Papaioannou, E. Salvadori, M. M. Roessler, G. Ploenes, E. R. H. van Eck, L. C. Tanase, J. Feng, Y. Sun, Y. Yang, M. Danaie, A. Belen Jorge, A. Sapelkin, J. Durrant, S. D. Dimitrov and M. M. Titirici, *ChemSusChem*, 2019, **12**, 4432–4441.
- X. Miao, D. Qu, D. Yang, B. Nie, Y. Zhao, H. Fan and Z. Sun, *Adv. Mater.*, 2018, **30**, 1704740.
- J. Yu, X. Yong, Z. Tang, B. Yang and S. Lu, *J. Phys. Chem. Lett.*, 2021, **12**, 7671–7687.
- B. Mehrdad-Vahdati, S. Pourhashem, M. Sedghi, Z. Vaezi, B. Shojaedin-Givi, A. Rashidi and H. Naderi-Manesh, *Toxicol. In Vitro*, 2019, **61**, 104649.
- S. Sahu, B. Behera, T. K. Maiti and S. Mohapatra, *Chem. Commun.*, 2012, **48**, 8835–8837.



- 9 Y. Liu, S. Roy, S. Sarkar, J. Xu, Y. Zhao and J. Zhang, *Carbon Energy*, 2021, **3**, 795–826.
- 10 Z. Xu, Z. Chen, T. Ji, D. Jv and P. Guan, *Mater. Lett.*, 2022, **309**, 131273.
- 11 A. Abbas, L. T. Mariana and A. N. Phan, *Carbon*, 2018, **140**, 77–99.
- 12 R. Wang, K. Q. Lu, Z. R. Tang and Y. J. Xu, *J. Mater. Chem. A*, 2017, **5**, 3717–3734.
- 13 P. Namdari, B. Negahdari and A. Eatemadi, *Biomed. Pharmacother.*, 2017, **87**, 209–222.
- 14 Y. Liu, H. Huang, W. Cao, B. Mao, Y. Liu and Z. Kang, *Mater. Chem. Front.*, 2020, **4**, 1586–1613.
- 15 P. Tian, L. Tang, K. S. Teng and S. P. Lau, *Mater. Today Chem.*, 2018, **10**, 221–258.
- 16 Z. Ji, E. Dervishi, S. K. Doorn and M. Sykora, *J. Phys. Chem. Lett.*, 2019, **10**, 953–959.
- 17 S. Zhu, Y. Song, J. Wang, H. Wan, Y. Zhang, Y. Ning and B. Yang, *Nano Today*, 2017, **13**, 10–14.
- 18 A. Bhattacharya, S. Chatterjee, R. Prajapati and T. Kanti Mukherjee, *Phys. Chem. Chem. Phys.*, 2015, 12833.
- 19 H. Ding, X.-H. Li, X.-B. Chen, J.-S. Wei, X.-B. Li and H.-M. Xiong, *J. Appl. Phys.*, 2020, **127**, 231101.
- 20 A. Sciortino, A. Cannizzo and F. Messina, *C*, 2018, **4**, 67.
- 21 W. Liu, Y. Han, M. Liu, L. Chen and J. Xu, *RSC Adv.*, 2023, **13**, 16232.
- 22 M. Langer, L. Zdražil, M. Medveď and M. Otyepka, *Nanoscale*, 2023, **15**, 4022–4032.
- 23 S. Y. Lim, W. Shen and Z. Gao, *Chem. Soc. Rev.*, 2015, **44**, 362–381.
- 24 K. J. Mintz, Y. Zhou and R. M. Leblanc, *Nanoscale*, 2019, **11**, 4634–4652.
- 25 S. Tao, T. Feng, C. Zheng, S. Zhu and B. Yang, *J. Phys. Chem. Lett.*, 2019, **10**, 5182–5188.
- 26 S. Tao, C. Zhou, C. Kang, S. Zhu, T. Feng, S. T. Zhang, Z. Ding, C. Zheng, C. Xia and B. Yang, *Light: Sci. Appl.*, 2022, **11**, 56–66.
- 27 X. Wang, G. Sun, P. Routh, D.-H. Kim, W. Huang and P. Chen, *Chem. Soc. Rev.*, 2014, **43**, 7067–7098.
- 28 X. Zhai, P. Zhang, C. Liu, T. Bai, W. Li, L. Dai and W. Liu, *Chem. Commun.*, 2012, **48**, 7955–7957.
- 29 Z. Qian, J. Ma, X. Shan, H. Feng, L. Shao and J. Chen, *Chem. – Eur. J.*, 2014, **20**, 2254–2263.
- 30 T. C. Wareing, P. Gentile and A. N. Phan, *ACS Nano*, 2021, **15**, 15471.
- 31 N. Tejwan, S. K. Saha and J. Das, *Adv. Colloid Interface Sci.*, 2020, **275**, 102046.
- 32 H. Ababneh and B. H. Hameed, *Int. J. Biol. Macromol.*, 2021, **186**, 314–327.
- 33 F. Yan, Y. Jiang, X. Sun, Z. Bai, Y. Zhang and X. Zhou, *Microchim. Acta*, 2018, **185**, 424–458.
- 34 A. Marinovic, L. S. Kiat, S. Dunn, M. M. Titirici and J. Briscoe, *ChemSusChem*, 2017, **10**, 1004–1013.
- 35 Q. Jiang, Y. Jing, Y. Ni, R. Gao and P. Zhou, *Microchem. J.*, 2020, **157**, 105111.
- 36 G. Gedda, C.-Y. Lee, Y.-C. Lin and H. Wu, *Sens. Actuators, B*, 2016, **224**, 396–403.
- 37 L. Cao, K. A. Shiral Fernando, W. Liang, A. Seilkop, L. Monica Veca, Y.-P. Sun and C. E. Bunker, *J. Appl. Phys.*, 2019, **125**, 220903.
- 38 V. P. Santos, N. S. S. Marques, P. C. S. V. Maia, M. A. B. de Lima, L. de, O. Franco and G. M. de Campos-Takaki, *Int. J. Mol. Sci.*, 2020, **21**, 1–17.
- 39 N. Papaioannou, M. M. Titirici and A. Sapelkin, *ACS Omega*, 2019, **4**, 21658.
- 40 C. Xia, J. Zhong, X. Han, S. Zhu, Y. Li, H. Liu and B. Yang, *Angew. Chem., Int. Ed.*, 2024, **63**, e202410519.
- 41 F. Rigodanza, M. Burian, F. Arcudi, L. Đorđević, H. Amenitsch and M. Prato, *Nat. Commun.*, 2021, **12**, 2640.
- 42 C. Xia, S. Zhu, T. Feng, M. Yang and B. Yang, *Adv. Sci.*, 2019, **6**, 1901316.
- 43 A. Weisstuch and A. C. Testa, *J. Phys. Chem.*, 1968, **72**, 1982–1987.
- 44 B. Y. Yubin Song, S. Zhu, S. Zhang, Y. Fu, L. Wang and X. Zhao, *Mater. Chem. C*, 2015, **3**, 5976.
- 45 H. Huang, K. Nishi, H. J. Tsai and B. D. Hammock, *Anal. Biochem.*, 2007, **363**, 12–21.
- 46 M. Royle, B. Chachuat, B. Xu and E. A. Gibson, *RSC Sustainability*, 2024, **2**, 1337–1349.
- 47 A. S. Nizami, M. Rehan, M. Waqas, M. Naqvi, O. K. M. Ouda, K. Shahzad, R. Miandad, M. Z. Khan, M. Syamsiro, I. M. I. Ismail and D. Pant, *Bioresour. Technol.*, 2017, **241**, 1101–1117.
- 48 J. Sherwood, *Bioresour. Technol.*, 2020, **300**, 122755.
- 49 R. E. Guedes, A. S. Luna and A. R. Torres, *J. Anal. Appl. Pyrolysis*, 2018, **129**, 134–149.
- 50 X. Gao, X. Chen, J. Zhang, W. Guo, F. Jin and N. Yan, *ACS Sustainable Chem. Eng.*, 2016, **4**, 3912–3920.
- 51 N. Ullal, R. Mehta and D. Sunil, *Analyst*, 2024, **149**, 1680–1700.
- 52 C. Dong, M. Xu, S. Wang, M. Ma, O. U. Akakuru, H. Ding, A. Wu, Z. Zha, X. Wang and H. Bi, *J. Nanobiotechnol.*, 2021, **19**, 1–8.
- 53 C. D. Yaqian Feng, R. Li and P. Zhou, *Microchem. J.*, 2022, **180**, 107627.
- 54 M. Jia, L. Peng, M. Yang, H. Wei, M. Zhang and Y. Wang, *Carbon*, 2021, **182**, 42–50.
- 55 H. Luo, L. Lari, H. Kim, S. Herou, L. C. Tanase, V. K. Lazarov and M. M. Titirici, *Nanoscale*, 2022, **14**, 910–918.
- 56 J. Zhan, R. Peng, S. Wei, J. Chen, X. Peng and B. Xiao, *ACS Omega*, 2019, **4**, 22574.
- 57 M. Feng, Y. Wang, B. He, X. Chen and J. Sun, *ACS Appl. Nano Mater.*, 2022, **5**, 7502–7511.
- 58 C. Klinke, R. Kurt, J. M. Bonard and K. Kern, *J. Phys. Chem. B*, 2002, **106**, 11191.
- 59 S. Lu, L. Sui, M. Wu, S. Zhu, X. Yong and B. Yang, *Adv. Sci.*, 2019, **6**, 1801192.
- 60 F. Ehrat, S. Bhattacharyya, J. Schneider, A. Löf, R. Wyrwich, A. L. Rogach, J. K. Stolarczyk, A. S. Urban and J. Feldmann, *Nano Lett.*, 2017, **17**, 7710–7716.
- 61 M. Ayiania, M. Smith, A. J. R. Hensley, L. Scudiero, J. S. McEwen and M. Garcia-Perez, *Carbon*, 2020, **162**, 528–544.
- 62 J. Briscoe, A. Marinovic, M. Sevilla, S. Dunn and M. Titirici, *Angew. Chem., Int. Ed.*, 2015, **54**, 4463–4468.
- 63 L. Zhao, Y. Wang, X. Zhao, Y. Deng and Y. Xia, *Polymers*, 2019, **11**, 1731–1743.



- 64 S. Liao, X. Zhao, F. Zhu, M. Chen, Z. Wu, X. Song, H. Yang and X. Chen, *Talanta*, 2018, **180**, 300–308.
- 65 Y. Ni, P. Zhou, Q. Jiang, Q. Zhang, X. Huang and Y. Jing, *Dyes Pigm.*, 2022, **197**, 109923.
- 66 Y. Chen, C. Zhao, Y. Wang, H. Rao, Z. Lu, C. Lu, Z. Shan, B. Ren, W. Wu and X. Wang, *Mater. Sci. Eng., C*, 2020, **117**, 111264.
- 67 Y. Xiong, J. Schneider, C. J. Reckmeier, H. Huang, P. Kasák and A. L. Rogach, *Nanoscale*, 2017, **9**, 11730.
- 68 M. Sudolská, M. Dubecký, S. Sarkar, C. J. Reckmeier, R. Zbořil, A. L. Rogach and M. Otyepka, *J. Phys. Chem. C*, 2015, **119**, 13369.
- 69 W. Kwon, S. Do, J. H. Kim, M. Seok Jeong and S. W. Rhee, *Sci. Rep.*, 2015, **5**, 12604.
- 70 Z. Liang, M. Kang, G. F. Payne, X. Wang and R. Sun, *ACS Appl. Mater. Interfaces*, 2016, **8**, 17478.
- 71 Y. Song, S. Zhu, S. Zhang, Y. Fu, L. Wang, X. Zhao and B. Yang, *J. Mater. Chem. C*, 2015, **3**, 5976–5984.
- 72 H. Yoon, Y. H. Chang, S. H. Song, E. S. Lee, S. H. Jin, C. Park, J. Lee, B. H. Kim, H. J. Kang, Y. H. Kim and S. Jeon, *Adv. Mater.*, 2016, **28**, 5255–5261.
- 73 S. H. Song, M. Jang, J. Chung, S. H. Jin, B. H. Kim, S. Hur, S. Yoo, Y. Cho and S. Jeon, *Adv. Opt. Mater.*, 2014, **2**, 1016–1023.
- 74 F. Yuan, T. Yuan, L. Sui, Z. Wang, Z. Xi, Y. Li, X. Li, L. Fan, Z. Tan, A. Chen, M. Jin and S. Yang, *Nat. Commun.*, 2018, **9**, 2249–2260.
- 75 F. Yuan, Z. Wang, X. Li, Y. Li, Z. Tan, L. Fan and S. Yang, *Adv. Mater.*, 2024, **36**, 2312060–2312063.

